Crystal structure of the dynamin tetramer

Reubold, T.F., Faelber, K., Plattner, N., Posor, Y., Ketel, K., Curth, U., Schlegel, J., Anand, R., Manstein, D.J., Noe, F., Haucke, V., Daumke, O., Eschenburg, S.

Nature
2015 SEP 17 ; 525(7569): 404-408
doi : 10.1038/nature14880
Nature Publishing Group

Crystal structure of the dynamin tetramer

Thomas F. Reubold[1*], Katja Faelber[2*], Nuria Plattner[3§], York Posor[4§], Katharina Branz[4], Ute Curth[1,5], Jeanette Schlegel[2], Roopsee Anand[1], Dietmar J. Manstein[1,5], Frank Noé[3], Volker Haucke[4,6], Oliver Daumke[2,6] & Susanne Eschenburg[1]

[1]*Medizinische Hochschule Hannover, Institut für Biophysikalische Chemie, Carl-Neuberg-Str. 1, 30625 Hannover, Germany*

[2]*Max-Delbrück-Centrum für Molekulare Medizin, Kristallographie, Robert-Rössle-Straße 10, 13125 Berlin, Germany*

[3]*Freie Universität Berlin, Institut für Mathematik, Arnimallee 6, 14195 Berlin, Germany*

[4]*Leibniz-Institut für Molekulare Pharmakologie, Robert-Rössle-Straße 10, 13125 Berlin, Germany*

[5]*Medizinische Hochschule Hannover, Forschungseinrichtung Strukturanalyse, Carl-Neuberg-Str. 1, 30625 Hannover, Germany*

[6]*Freie Universität Berlin, Institut für Chemie und Biochemie, Takustraße 6, 14195 Berlin, Germany*

* These authors contributed equally to this work.

§ These authors contributed equally to this work.

The mechano-chemical protein dynamin is the prototype of the dynamin superfamily of large GTPases, which shape and remodel membranes in diverse cellular processes[1]. Dynamin forms predominantly tetramers in the cytosol, which oligomerize at the neck of clathrin-coated vesicles to mediate constriction and subsequent scission of the membrane[1]. Previous studies have described the architecture of dynamin dimers[2,3], but the molecular determinants for dynamin assembly and its regulation have remained unclear. Here, we present the crystal structure of the nucleotide-free dynamin tetramer. Combining structural data with mutational studies, oligomerization measurements and molecular dynamics simulations, we suggest a mechanism of how oligomerization of dynamin is linked to the release of intramolecular auto-inhibitory interactions. We elucidate how mutations that interfere with tetramer formation and auto-inhibition can lead to the congenital diseases Charcot-Marie-Tooth neuropathy (CMT)[4] and centronuclear myopathy (CNM)[5], respectively. Strikingly, the bent shape of the tetramer explains how dynamin assembles into a right-handed helical oligomer of defined diameter, which has direct implications for its function in membrane constriction.

The three highly conserved vertebrate isoforms of dynamin contain five distinct domains (Extended Data Fig. 1a): an N-terminal GTPase (G) domain mediating nucleotide binding and hydrolysis, a bundle signaling element (BSE), a stalk, a pleckstrin homology (PH) domain involved in lipid binding, and a proline rich domain (PRD) mediating interaction with BAR- and SH3-domain containing scaffolding proteins[6]. To exert its function in clathrin-mediated endocytosis (CME), dynamin assembles via the stalks into a helical array surrounding the necks of invaginating clathrin-coated pits (CCP)[7,8]. Dimerization of GTP-bound G domains from neighboring helical rungs induces GTP hydrolysis[9]. The ensuing conformational changes are thought to be transmitted from the G domain via the BSE to the stalk resulting in a sliding motion of adjacent helix rungs, concomitant helix constriction[10], and eventually membrane scission. The inherent tendency to form large assemblies at high protein concentrations has hampered crystallization of dynamin in the past. The use of non-

oligomerizing mutants led to crystal structures of dynamin 1[2,3]. However, the postulated higher-order assembly interface was not resolved in these structures leaving the oligomerization mechanism unaddressed.

We reasoned that an alternative assembly-affecting mutation, such as K361S in dynamin 3[11], may disturb the oligomerization interface to a lesser extent than the previously used mutants. We obtained crystals of nucleotide-free dynamin 3-K361S lacking the PRD (dynamin 3(ΔPRD)-K361S) that diffracted to 3.7 Å (Methods, Extended Data Fig. 1, Extended Data Table 1). Indeed, the asymmetric unit of the crystal lattice contained a dynamin tetramer that did not form the filamentous superstructures seen for dynamin 1[2,3].

The dynamin tetramer is built of two dimers. Each of the dimers assembles via the previously described interface 2[2,3,12-14] (Fig. 1, Extended Data Fig. 2a, b). Different dimerization and assembly models were derived from EM reconstructions and cross-linking experiments[9]. These models, however, are not compatible with the architecture of the dynamin tetramer (Extended Data Fig. 2c). To provide further evidence for dimerization via interface 2, we introduced the triple mutation I481D/H677D/L678S into dynamin 3(ΔPRD) and the corresponding mutation (I481D/H687D/L688S) into dynamin 1(ΔPRD). These mutants were monomeric in AUC experiments (Extended Data Fig. 2d). Thus, dimerization via interface 2 is indeed a general feature of dynamin and dynamin-like proteins. This conclusion receives additional support from recent cross-linking data[15].

Dynamin 3 dimers further assemble into tetramers via interface 1 and interface 3 (Fig. 1, Extended Data Fig. 3a). Interface 1 at the top of the stalk features four hydrophobic residues that are highly conserved in the dynamin superfamily (Fig. 1; Supplementary Fig. 1). The main contributors for interface 3 are loop $L1N^S$ of the inner and loop $L2^S$ of the outer stalks (Fig. 1) which mediate an intricate interaction network involving all four stalks (Extended Data Fig. 3a). Accordingly, these loops are well defined in the inter-dimer interface (Extended Data Fig. 3b), but not at the outer, non-assembled sides of the tetramer. Previous

studies have shown that mutation of R399 in loop $L2^S$ completely destroys higher-order assembly and dynamin function[2,3,11]. In our structure, R399 of an outer molecule forms salt bridges to E410 in $\alpha2^S$ and to E345 in $L1N^S$ in the outer and inner molecules of the opposite dimer, respectively. In the hydrophobic core of interface 3, L402 and F403 in $L2^S$ of outer molecules interact with F493, F496, L655 and T651 of outer molecules in the neighboring dimer (Fig. 1 and Extended Data Fig. 3a). Mutation of F403 and of E410 yielded predominantly dimeric protein and compromised liposome binding as well as liposome-stimulated GTPase activity (Fig. 2a-c). In dynamin 2, the F403A mutation substantially interfered with CME, as monitored by transferrin internalization (Fig. 2d). The effect of E410A on CME was less pronounced (Fig. 2d), since the structural defect may in part be compensated by the second salt bridge that R399 forms to E345 (Fig. 1, Extended Data Fig. 3a).

$L1N^S$ of an inner stalk also interacts with $\alpha1C^S$ of an outer stalk. Accordingly, mutation of N-terminal (SGD347-349AAA), central (QVDT350-353AAAA) or C-terminal (LELS354-357AAAA) residue stretches in $L1N^S$ interfered with tetramerization (Fig. 2a). The central and C-terminal, but not the N-terminal mutations compromised liposome binding and assembly-stimulated GTPase activity (Fig. 2b, c). The QVDT350-353AAAA mutant showed a reduced ability to sustain CME of transferrin, whereas the central LELS354-357AAAA mutant displayed a dominant-negative effect in transferrin uptake assays (Fig. 2d). The CMT-neuropathy related mutation G358R[16,17] is located in the C-terminus of $L1N^S$ (Extended Data Fig. 3c). This mutation led to a dimeric mutant that did not bind to liposomes (Fig. 2a-c). Likewise, it exhibited a dominant-negative effect on CME (ref. 16, 17 and Fig. 2d). The bulky arginine side chain likely interferes with the proper binding conformation of $L1N^S$. Interestingly, the mutants LELS354-357AAAA, G358R, and F403A, were still recruited to CCPs; these pits, however, remained stable at the membrane surface (Extended

Data Fig. 3d). Thus, dynamin's function at CCPs, but not its recruitment, depends on an intact interface 3.

The dimers in the dynamin tetramer are asymmetric concerning the PH domain and the orientation of the G domain and the BSE (Fig. 1). Compared to an 'outer' molecule, G domains of 'inner' molecules are tilted by approximately 40° around hinge 1 between the BSE and the stalk (Extended Data Fig. 4a). The PH domains of the outer molecules bind to a conserved surface of the stalk (Fig. 3a, b), to a similar site as in dimeric dynamin 1[2] (Extended Data Fig. 4b). The assignment of the visible PH domains to the outer molecules is unambiguous (Extended Data Fig. 4c). The PH domains of the inner molecules were not resolved in the electron density (Extended Data Fig. 4d). Modelling of the inner PH domains to positions equivalent to those observed for the outer molecules leads to clashes with the outer stalks (Fig. 3c, Extended Data Fig. 4e). Apparently, the PH domains have to be released from their auto-inhibitory site for oligomerization to proceed. In line with this assumption, a dynamin 3 variant lacking the PH domain assembled in the absence of membranes and in the presence of nucleotides more efficiently into regular oligomers than Wt dynamin 3 (Extended Data Fig 5a-c). Dynamin 3 tubulated liposomes on its own and did not need a specific membrane curvature for binding. At physiological salt concentrations, dynamin 3 efficiently bound to and tubulated unfiltered Folch liposomes (Extended Data Fig. 5d, e). This is in line with the presence of a tyrosine in position 596, which has been suggested to serve as determinant for curvature generation versus curvature sensing[18]. When expressed in mammalian cells, dynamin 2(ΔPH) formed large, presumably cytosolic aggregates that failed to colocalize with clathrin and interfered with transferrin uptake in a dominant-negative fashion (Extended Data Fig. 5f, g), as has been shown previously for dynamin 1[19]. These results indicate that the PH domain has important functions in oligomerization and membrane binding.

To investigate this dual function of the PH domain, we inserted the mutations R364S, R518H, R518D, and E355A into the interface between PH domain and stalk (Extended Data Fig. 6). Similar to nearby interface-3 mutants, most of these mutations impeded assembly, liposome binding, liposome-stimulated GTPase activity and transferrin uptake. In contrast, the mutation R518D enhanced oligomerization and GTP hydrolysis, as previously described for mutants in the PH domain stalk interface[2,20].

Molecular dynamics (MD) simulations were carried out and analyzed by Markov models[21-23] to characterize the dynamics of the PH domain stalk interface and the interplay with interface 3 (Fig. 3, Extended Data Fig. 7). The simulations showed that E355 and K361, together with R518 and R364, are part of a network of polar interactions (Extended Data Fig. 7a) that can rapidly interconvert leading to three distinct binding modes (Fig. 3c). The preferred binding conformation of the PH domain to the stalk was the auto-inhibitory 'closed' interaction found in our crystals. In two other 'open' conformations, the PH domain was shifted along the stalk to a position, where it did not interfere with oligomerization, indicating a dynamic equilibrium of oligomerization-permissive and non-permissive binding modes. The mutation K361S resulted in the appearance of a fourth, highly populated conformation that was also auto-inhibitory for oligomerization, whereas no oligomerization-permissive binding modes were detected (Fig. 3c, d). Further MD simulations and Markov models of the stalk with dissociated PH domain indicated that the mutant K361S predominantly stabilizes the loop $L1N^S$ in a conformation that is not adopted in the wild-type (Extended Data. Fig. 7c). Together, these results may explain the reduced oligomerization capacity of K361S, which is dimeric in solution (Extended Data Fig. 6c). Apparently, a set of highly conserved charged residues including K361 regulates both the auto-inhibitory interaction with the PH domain and interactions with $L1N^S$, thereby tightly coupling auto-inhibition and oligomerization.

Comparison of the dynamin tetramer with the filament-like arrangements observed in the crystal structures of dynamin 1[2,3] shows that the tetramer is bent, such that the angle

between the outer stalks is changed by 20° (Fig. 1, 4a). We constructed a dynamin oligomer by stepwise adding tetramers to the free ends of the growing dynamin assembly, using the geometry of interface 3 to connect the tetramers. This leads to a right-handed helix (Fig. 4b), closely matching the dimensions of the dynamin 1 helix in the non-constricted, nucleotide-free state[24]. These observations indicate that formation of a right-handed dynamin helix at the surface of a tubular membrane is an intrinsic feature of stalk assembly via interface 3. The bent shape of the tetramer appears to dictate the curvature of a membrane tubule around which dynamin preferentially oligomerizes[24,25]. Constriction of membrane tubules to inner diameters smaller than 16 nm requires active GTP turnover and the associated G domain interactions across helical turns. Comparison of our structure with a recent cryo-EM model of a super-constricted dynamin helix[26] (Extended Data Fig. 2c) suggests that constriction of the dynamin helix is driven via conformational changes in the stalk interfaces.

The stalks of our helix model fit well into a cryo-EM map of nucleotide-free dynamin 1 assembled around a lipid tubule[24] (Fig. 4b), but the PH domains and the G domains protrude from the electron density (Fig. 4a, Extended Data Fig. 8a). Apparently, the PH domains are shed from the auto-inhibitory stalk interface to bind the membrane tubule whereas the G domains move upwards from their positions. To explain dynamin's assembly, we propose an equilibrium between PH domains bound (as seen for the outer molecules) and unbound (as for the inner molecules) to their stalks. In the cytosol, this equilibrium lies to the autoinhibited tetramer to prevent untimely oligomerization. CNM-related mutations in the interface between stalk and PH domain (Fig. 3b, Extended Data Fig. 9) shift the equilibrium towards the oligomerized state, thereby leading to disease. Upon dynamin recruitment by accessory proteins to endocytic sites, the equilibrium is driven towards the assembly-competent conformation. This hypothesis is supported by studies showing that *in vivo*, dynamin helices are built by incorporation of dimer or tetramer units rather than larger preformed dynamin assemblies[27,28]. Further interactions, which may influence the assembly equilibrium, occur

between BSE and stalk and G domain and PH domain of adjacent dimers (Extended Data Figure 8b-d). In this view, the effect of the disease-relevant mutation R465W may be explained. In the tetramer, R465 of an outer molecule is in close vicinity to the inner BSE of an adjacent dimer and a tryptophan at this position is likely to modify this interaction resulting in enhanced oligomerization.

A striking feature of dynamin assembly is the multitude of interactions in all four molecules of the tetramer (Extended Data Fig. 3a). Our results indicate that these contacts are not necessarily static, but are characterized by a dynamic equilibrium of different binding conformations. The formation of new interactions during assembly is compensated by the release of auto-inhibitory contacts in the dynamin tetramer. Such an assembly mode that involves many low affinity interaction sites facilitates reversibility and allows regulation, for example via nucleotide binding, hydrolysis or phosphorylation[29]. It is the basis for the particular interaction mode of the semi-solid dynamin polymer with its protein and membrane environment, which has been previously identified in other CME proteins and has been coined as 'matricity'[30].

Online Content Methods, along with any additional Extended Data display items, are available in the online version of the paper; references unique to these sections appear only in the online paper.

References

1. Ferguson, S. M. and De Camilli, P., Dynamin, a membrane-remodelling GTPase. *Nat Rev Mol Cell Biol* **13**, 75-88 (2012).
2. Faelber, K. et al., Crystal structure of nucleotide-free dynamin. *Nature* **477**, 556-560 (2011).
3. Ford, M. G., Jenni, S., and Nunnari, J., The crystal structure of dynamin. *Nature* **477**, 561-566 (2011).
4. Cowling, B. S., Toussaint, A., Muller, J., and Laporte, J., Defective membrane remodeling in neuromuscular diseases: insights from animal models. *PLoS Genet* **8**, e1002595 (2012).

5. Durieux, A. C., Prudhon, B., Guicheney, P., and Bitoun, M., Dynamin 2 and human diseases. *J Mol Med* **88**, 339-350 (2010).
6. Daumke, O., Roux, A., and Haucke, V., BAR domain scaffolds in dynamin-mediated membrane fission. *Cell* **156**, 882-892 (2014).
7. Hinshaw, J. E. and Schmid, S. L., Dynamin self-assembles into rings suggesting a mechanism for coated vesicle budding. *Nature* **374**, 190-192 (1995).
8. Takei, K., McPherson, P. S., Schmid, S. L., and De Camilli, P., Tubular membrane invaginations coated by dynamin rings are induced by GTP-gamma S in nerve terminals. *Nature* **374**, 186-190 (1995).
9. Chappie, J. S. et al., A pseudoatomic model of the dynamin polymer identifies a hydrolysis-dependent powerstroke. *Cell* **147**, 209-222 (2011).
10. Faelber, K. et al., Structural insights into dynamin-mediated membrane fission. *Structure* **20**, 1621-1628 (2012).
11. Ramachandran, R. et al., The dynamin middle domain is critical for tetramerization and higher-order self-assembly. *EMBO J* **26**, 559-566 (2007).
12. Frohlich, C. et al., Structural insights into oligomerization and mitochondrial remodelling of dynamin 1-like protein. *EMBO J* **32**, 1280-1292 (2013).
13. Gao, S. et al., Structure of myxovirus resistance protein a reveals intra- and intermolecular domain interactions required for the antiviral function. *Immunity* **35**, 514-525 (2011).
14. Gao, S. et al., Structural basis of oligomerization in the stalk region of dynamin-like MxA. *Nature* **465**, 502-506 (2010).
15. Srinivasan, S., Mattila, J. P., and Schmid, S. L., Intrapolypeptide Interactions between the GTPase Effector Domain (GED) and the GTPase Domain Form the Bundle Signaling Element in Dynamin Dimers. *Biochemistry* **53**, 5724-5726 (2014).
16. Koutsopoulos, O. S. et al., Mild functional differences of dynamin 2 mutations associated to centronuclear myopathy and Charcot-Marie Tooth peripheral neuropathy. *PLoS One* **6**, e27498 (2011).
17. Sidiropoulos, P. N. et al., Dynamin 2 mutations in Charcot-Marie-Tooth neuropathy highlight the importance of clathrin-mediated endocytosis in myelination *Brain* **135**, 1395-1411 (2012).
18. Liu, Y. W. et al., Differential curvature sensing and generating activities of dynamin isoforms provide opportunities for tissue-specific regulation *Proc Natl Acad Sci U S A* **108**, E234-E242 (2011).
19. Vallis, Y. et al., Importance of the pleckstrin homology domain of dynamin in clathrin-mediated endocytosis *Curr Biol* **9**, 257-260 (1999).
20. Kenniston, J. A. and Lemmon, M. A., Dynamin GTPase regulation is altered by PH domain mutations found in centronuclear myopathy patients. *EMBO J* **29**, 3054-3067 (2010).
21. Bowman, G. R., Pande, V. S., Noé, F.,editors, *An Introduction to Markov State Models and Their Application to Long Timescale Molecular Simulation.* (Springer, 2014).
22. Schütte, C. and Sarich, M., Metastability and Markov models in molecular dynamics: modeling, analysis, algorithmic approaches *Courant Lecture Notes (American Mathematical Society)* **24**, 128 pp. (2013).
23. Kohlhoff, K. J. et al., Cloud-based simulations on Google Exacycle reveal ligand modulation of GPCR activation pathways *Nat Chem* **6**, 15-21 (2014).
24. Chen, Y. J., Zhang, P., Egelman, E. H., and Hinshaw, J. E., The stalk region of dynamin drives the constriction of dynamin tubes. *Nat Struct Mol Biol* **11**, 574-575 (2004).

25. Roux, A. et al., Membrane curvature controls dynamin polymerization. *Proc Natl Acad Sci U S A* **107**, 4141-4146 (2010).
26. Sundborger, A. C. et al., A dynamin mutant defines a superconstricted prefission state *Cell Rep* **8**, 734-742 (2014).
27. Cocucci, E., Gaudin, R., and Kirchhausen, T., Dynamin recruitment and membrane scission at the neck of a clathrin-coated pit *Mol Biol Cell* **25**, 3595-3609 (2014).
28. Grassart, A. et al., Actin and dynamin2 dynamics and interplay during clathrin-mediated endocytosis *J Cell Biol* **205**, 721-735 (2014).
29. Graham, M. E., O'Callaghan, D. W., McMahon, H. T., and Burgoyne, R. D., Dynamin-dependent and dynamin-independent processes contribute to the regulation of single vesicle release kinetics and quantal size *Proc Natl Acad Sci U S A* **99**, 7124-7129 (2002).
30. Schmid, E. M. and McMahon, H. T., Integrating molecular and network biology to decode endocytosis. *Nature* **448**, 883-888 (2007).

Supplementary Information is linked to the online-version of the paper at **www.nature.com/nature**.

Acknowledgements. This project was supported by grants from the Deutsche Forschungsgemeinschaft (MA1081/8-2 to D.J.M, SFB740/D7 and SFB958/A04 to F.N., SFB740/C8, and SFB 958/A7 to V.H., SFB 740/C7 and SFB958/A12 to O.D., ES410/2-1 to S.E.), an ERC consolidator grant (ERC-2013-CoG-616024 to O.D.), an ERC starting grant (pcCell to F.N.) and a grant from the Einstein foundation Berlin (SOoPiC to N.P.). T.F.R. acknowledges partial financial support by the Cluster of Excellence REBIRTH (DFG EXC 61/1). We thank B. Purfürst for help with electron microscopy. We thank Sophie Hertel, Lidia Litz, Petra Straub and Sabine Wohlgemuth for experimental assistance and the staff at beamlines X06SA (PXI) and X06DA (PXIII) at the Swiss Light Source (Villigen, Switzerland) for help during data collection. We thank Ya-Wen Liu for helpful discussions and Alfred Wittinghofer for his generous support and inspiring discussions in the initial stages of the project.

Author contribution. T.F.R. grew the crystals and collected data, K.F. solved the structure, T.F.R., K.F. and S.E. refined the structure, T.F.R. and R.A. purified protein for crystallization and monomeric dynamin, K.F. and J.S. purified all other proteins, performed liposome co-sedimentation, EM and GTPase assays, U.C. performed and analyzed AUC experiments, Y.P. and K.B. performed transferrin uptake assays, N.P. and. F.N. conducted and analyzed molecular modeling and molecular dynamics simulations. T.F.R, K.F., F.N., V.H., O.D. and S.E. interpreted structural data. T.F.R., K.F., Y.P., N.P., U.C., D.J.M., F.N., V.H., O.D. and S.E. designed research, T.F.R., K.F., F.N., O.D. and S.E. wrote the manuscript.

Author information. The atomic coordinates and structure factors of human dynamin3 have been deposited in the Protein Data Bank with accession number 5A3F. Reprints and permission information is available at npg.nature.com/reprintsandpermissions. The authors declare no competing financial interest.

Correspondence and requests for materials should be addressed to K.F. (katja.faelber@mdc-berlin.de), O.D. (oliver.daumke@mdc-berlin.de), or S.E. (Eschenburg.Susanne@mh-hannover.de).

Methods

Protein expression and purification. Human dynamin 3 (splice form abb[31], residues 1-754) and indicated mutants of this construct were expressed from pProEx-HTb (Invitrogen) as N-terminal His_6-tag fusion followed by a tobacco etch virus (TEV) cleavage site. The crystallized construct contained the K361S mutation. Proteins were produced in *Escherichia coli* host strain BL21(DE3), and expression was induced by addition of 0.1 mM isopropyl-β-D-thiogalactopyranoside (IPTG). Cells were grown over night at 20 °C in TB medium. The following procedure was used for purification of dynamin 3 K361S for crystallization. Cells were resuspended in buffer A300 (50 mM HEPES/NaOH (pH 7.5), 300 mM NaCl, 15 mM Imidazole, 2 mM $MgCl_2$) including 1 mM phenylmethylsulfonylfluoride (PMSF) and 0.1% v/v NP-40 and disrupted by sonification. Cleared lysates (30,000 g, 1 h, 4 °C) were applied to a Ni^{2+}-NTA column (Qiagen). The column was sequentially washed with buffer A300 and with buffer A100 (100 mM NaCl). Protein was eluted with buffer A100 containing additional 285 mM imidazole. Fractions containing human dynamin 3 were pooled and diluted with an equal volume of 50 mM HEPES/NaOH (pH 7.5). The diluted protein was loaded onto a HiLoad SuperQ anion exchange column (GE Healthcare) equilibrated with buffer B50 (in which 50 refers to the NaCl concentration) containing 50 mM HEPES/NaOH (pH 7.5), 50 mM NaCl, 2 mM DTE, 1 mM $MgCl_2$. After washing with buffer B50, bound proteins were eluted with a linear gradient from 50 to 500 mM NaCl. Fractions containing human dynamin 3 were pooled, 1 mg TEV per 10 mg dynamin 3 was added, and the protein incubated on ice for 4 h. The solution was concentrated using 50 kDa molecular weight cut-off concentrators (Amicon) and applied onto a Superdex200 gel filtration column (GE Healthcare) equilibrated with buffer B100. Fractions containing dynamin 3 were pooled, concentrated and flash-frozen in liquid nitrogen.

Wt and mutant dynamin 3 used for biochemical and biophysical assays were expressed in E.coli Rosetta2-BL21-DE3 in autoinduction medium (Novagen) and purified using a Co^{2+}-

Talon column, followed by overnight TEV cleavage (4 °C, 30 µg per 1 mg fusion protein), dilution / concentration in concentrators for imidazole removal and a second Co^{2+}-Talon column run for His_6-TEV and uncleaved His_6-dynamin capture. Finally, the peak fractions from a Superdex200 gel filtration containing dynamin were pooled, concentrated to maximal 20 mg/ml and flash frozen in liquid nitrogen. The purification buffer contained 20 mM HEPES/NaOH, pH 7.8, 500 mM NaCl, and 2 mM $MgCl_2$ (plus 100 mM imidazole for elution, plus 2.8 mM β-Mercaptoethanol during TEV cleavage). The purified protein was nucleotide-free, as confirmed by HPLC analysis (see below for details).

Crystallization and structure determination. Crystallization trials by the sitting-drop vapor-diffusion method were performed at 4 °C using a mosquito LCP pipetting robot (TTP Labtech) and Rock Imager storage system (Formulatrix). 150 nl of the human dynamin 3 at a concentration of 20 mg/ml was mixed with an equal volume of reservoir solution from commercially available preformulated screens. On a preparative scale, 2 µl of protein solution was mixed with 2 µl of reservoir solution containing 100 mM MES/NaOH (pH 6.5) and 15 % MPD. Crystals appeared after three to five days and reached final dimensions of up to 0.5 mm × 0.3 mm × 0.3 mm. Crystals were cryo-protected by immersion in reservoir solution added with increasing amounts of ethylene glycol (EG) with the final solution containing 17 % v/v ethylene glycol. Cryo-protected crystals were flash-cooled in liquid nitrogen. Data were recorded at beamline PXI-X06SA at the Swiss Light Source (Villigen, Switzerland). Native data from a single crystal was processed and scaled using the program package XDS[32]. The structure was solved by molecular replacement with Phaser[33] using the structure of the nucleotide free rat dynamin 1 G domain (2AKA), the stalk of human dynamin (3SNH) and the human PH domain (1DYN) as search models. The model was built using COOT[34] and iteratively refined using Phenix[35] with NCS between the outer and the inner molecules, respectively, with reference model restraints against an artificial dynamin construct composed of the high resolution search model domains, and with 1 TLS parameter per domain.

Due to weak electron density, all residues of the G domains of the inner molecules were chopped at the Cβ atoms, and the whole domains were refined as rigid bodies. In the final model, the outer molecules have disordered regions in the $L1N^{S}$ loop, the $L1^{SP}$ and $L2^{SP}$ loops and the $L5^{P}$ loop, and the inner molecules in the hinge 1 region and the $L2^{S}$ loop. Furthermore, the complete PH domains of the inner molecules are not resolved in the electron density. The structure was refined to R_{work}/R_{free} of 23,2%/27.8%. 96.4% of all residues are in the most favored regions of the Ramachandran plot and 0.7% (17/2500) residues in the disallowed regions, as analyzed with Molprobity[36]. Figures were prepared with PyMOL[37]. Domain superpositions were performed with lsqkab[38]. Sequences were aligned using CLUSTAL W[39] and adjusted by hand. The model of the right-handed dynamin 3 helix was fitted manually into the EM map using PyMOL[37] and Chimera[40].

Analytical ultracentrifugation. Sedimentation velocity experiments (SV) were carried out in a Beckman Coulter ProteomeLab XL-I analytical ultracentrifuge at 35,000 rpm and 20 °C using an An-50 Ti rotor. Concentration profiles were measured using the manufacturer's data acquisition software ProteomeLab XL-I Version 6.0 (Firmware 5.7) with the absorption scanning optics at 280 nm. SV analysis was performed in a buffer containing 0.15 M NaCl, 50 mM HEPES/NaOH (pH 7.5) in 3 or 12 mm standard double sector centerpieces filled with 100 µl or 400 µl sample, respectively. For data analysis, a model for diffusion-deconvoluted differential sedimentation coefficient distributions (continuous c(s) distributions) implemented in the program SEDFIT[41] was used. For proteins sedimenting as a single species, molecular masses were obtained from c(s) analysis as calculated from s-value and diffusion broadening of the sedimenting boundary. Dynamin 3 (ΔPRD)-K361S/R399A mutant, analysed in a concentration range from 4-23 µM, showed a single peak in c(s) distributions with a sedimentation coefficient slightly decreasing with increasing protein concentration (data not shown). Due to hydrodynamic nonideality, this is expected for a protein that does not change its oligomerization state with concentration[42]. Extrapolation to

zero concentration yielded $s_{20,w}$ = 6.4 S and a molecular mass of 160 kDa was obtained from c(s) analysis. Since the molecular mass of the monomer as calculated from the amino acid composition is 86 kDa, this mutant forms dimers in solution. For comparison, all other mutants were analysed at a concentration of about 20 µM. The following molecular masses were obtained from c(s) analyses of mutants that sedimented as a single species: QVDT350-353AAAA 162 kDa; LELS354-357AAAA 164 kDa; G358R: 167 kDa.

Partial specific volume, buffer density and viscosity were calculated from amino acid and buffer composition, respectively, by the program SEDNTERP[43] and were used to correct experimental s-values to $s_{20,w}$. Figures were prepared using the program GUSSI (http://biophysics.swmed.edu/MBR/software.html, kindly provided by Dr. C. Brautigam).

Liposome co-sedimentation assays. Liposomes were prepared as previously described (www.endocytosis.org). Folch liposomes (total bovine brain lipids fraction I from Sigma) in 20 mM HEPES/NaOH (pH 7.5), 100 mM NaCl were 13X extruded through a 0.1 µm filter. 0.2 mg/ml liposomes were incubated at room temperature with 4.0 µM of the indicated dynamin 3 construct for 10 min in 40 µl reaction volume, followed by a 213,000 g spin for 10 min at 20 °C. The final reaction buffer contained 25 mM HEPES/NaOH pH 7.5, 140 mM NaCl, 2 mM $MgCl_2$, 1 mM KCl.

GTP hydrolysis assay. GTPase activities of 1 µM of the indicated dynamin constructs were determined at 37 °C in 25 mM HEPES/NaOH (pH 7.5), 130 mM NaCl, 2 mM $MgCl_2$, 1 mM KCl, in the absence and presence of 0.1 mg/ml 0.1 µm filtered Folch liposomes, using saturating concentrations of GTP as substrate (1 mM for the basal and 3 mM for the stimulated reactions). Reactions were initiated by the addition of protein to the reaction. At different time points, reaction aliquots were 15-fold diluted and quickly transferred to liquid nitrogen. Nucleotides in the samples were separated via a reversed-phase Hypersil ODS-2 C18 column (250 × 4 mm), with 100 mM potassium phosphate buffer pH 6.5, 10 mM tetrabutylammonium bromide, 7.5% acetonitrile as running buffer. Denatured proteins were

adsorbed at a C18 guard column. Nucleotides were detected by absorption at 254 nm and quantified by integration of the corresponding peaks. Rates were derived from a linear fit to the initial reaction (< 20% GTP hydrolyzed).

Electron microscopy. For electron microscopic studies (Zeiss EM910), 2 µM dynamin 3 in 25 mM HEPES/NaOH (pH 7.5), 60 or 150 mM NaCl, 2 mM $MgCl_2$, 1 mM KCl and 1 mM guanosine-5'-[(β,γ)-methyleno]triphosphate (GMPPCP) were incubated at room temperature for 20 h without liposomes or for 20 min with liposomes. The final concentration of unfiltered liposomes was 0.35 mg/ml. Samples were spotted on carbon-coated copper grids (Plano GmbH, Wetzlar) and negatively stained with 3% uranyl acetate.

Transferrin uptake in HeLa cells. HeLa cells were transfected with siRNA using Oligofectamine (Invitrogen). The sequence of the siRNA targeting human dynamin2 is 5`-GCAACUGACCAACCACAUC-3` (nucleotides 849 – 867). After 24 h, cells were transfected with pEGFP-N1 (Clontech) or siRNA-resistant rat dynamin2-pEGFP-N1 using lipofectamine 2000 (Invitrogen). 72 h after siRNA-transfection, cells were serum-starved for 1 hour and incubated with 15 µg/ml transferrin-Alexa647 (Molecular Probes, Invitrogen) for 10 min at 37 °C. On ice, cells were washed once with cold PBS + 10 mM $MgCl_2$ and once for 90 s with 0.1 M acetic acid pH 5.3, 200 mM NaCl to remove surface-bound transferrin. After two washes with cold PBS + 10 mM $MgCl_2$, cells were detached from the culture dish by incubating for 5 min on ice with 0.1% PronaseE solution in PBS + 0.5 mM EDTA. Cells were resuspended in 1% bovine serum albumin (BSA) in PBS, pelleted at 300g for 5 min at 4 °C and fixed in 4% PFA, 4% sucrose in PBS for 15 min on ice and another 20 min at room temperature. Cells were pelleted and resuspended in 1% BSA in PBS and analyzed by flow cytometry using a BD FACScalibur. Transferrin fluorescence in GFP-positive cells was quantified and normalized to cells rescued with Wt dynamin2-eGFP.

Localization of dynamin2-eGFP mutants and analysis of clathrin-coated pit dynamics. HeLa cells depleted of endogenous dynamin 2 as described above were co-transfected with

plasmids encoding eGFP or dynamin2-eGFP and mRFP-clathrin light chain. 72 h after siRNA transfection, cells were analyzed by total internal reflection fluorescence (TIRF) microscopy using a Nikon Eclipse Ti (Andor sCMOS camera, Okolab incubator, Nikon PerfectFocus autofocus system, 60x TIRF-objective, operated by open source ImageJ-based Micromanager software[44]. For live imaging, cells growing on glass coverslips were kept in Hank's balanced salt solution + 5% fetal bovine serum. From 180 s dual-color TIRF recordings with a frame rate of 0.5 Hz, kymographs were created by selecting a line of pixels from an individual cell and depicting this line over the duration of 90 frames.

Molecular dynamics simulation and modelling. Molecular dynamics (MD) simulations of the stalk and the pleckstrin homology (PH) domain (residues 322 to 710) were carried out for the Wt and the K361S mutant, each using three different setups:

- Setup 1) The crystal structure coordinates of chain C superimposed to chain B were taken as starting point.
- Setup 2) Starting from setup 1 the PH domain was moved 5 Å away from the stalk.
- Setup 3) The PH domain was absent.

Setups 1 and 2 were used in order to study the conformational equilibrium of PH-stalk domain interactions. The loops joining the stalk to the PH domain (residues 495 to 511 and 628 to 640) were generated for each setup and mutant using VMD[45] and were minimized and equilibrated separately. The aim of the setup 3 was to study the intrinsic conformational dynamics of the $L1N^S$ loop when the PH domain is dissociated from the stalk.

The coordinates of each setup and for each mutant were used to construct an all-atom molecular model and run MD simulations in explicit solvent with GROMACS[46] using the CHARMM27 force field[47]. Setup and equilibration procedure: hydrogen atoms were added based on the heavy atom coordinates followed by an initial energy minimization. The protein was then solvated in water box with an at least 10 Å solvation layer, resulting in an overall system of between 70,000 and 80,000 atoms (depending on the initial structure). Na^+ and Cl^-

ions (100 mM) were added in order to buffer the system and obtain an overall neutral simulation cell. The solvated and ionized system was then again minimized and equilibrated in the NVT ensemble at 300 K with position constrains on the protein heavy atoms. A second equilibration was carried out in the NPT ensemble, again with position constrains, followed by a 1 ns equilibration without constrains. The equilibrated coordinates and velocities were used as the starting point for 20 100-ns production runs for each setup and with both wild-type and mutant K361S, giving rise to a total of 12 microseconds of molecular dynamics data.

Analysis with Markov state models. The conformations of the L1N^S loop and the stalk-PH domain patterns can be well characterized by their hydrogen bonding patterns within the loop or between stalk and PH domains. Here, 21 residue pairs, shown in Extended Data Figure 7d, were selected that can form hydrogen bonds or salt bridges. The Cα-distances of these residue pairs were evaluated in order to obtain a low-dimensional representation of the respective configuration. These distances were used to build Markov state models (MSMs)[21-23,48,49] of Setup 3 (L1N^S loop) and using both setups 1 and 2 for the PH-Stalk interactions using the EMMA program[50] (http://pyemma.org). The microstates of the MSMs were obtained by regular spatial clustering in the distance space[48]. The distance cutoff for the regular spatial clustering was chosen to obtain around 500 microstates. Using a cutoff of 10.75 Å for the wild type and a cutoff of 9 Å for the mutant K361S resulted in 550 and 584 microstates, respectively. The lag time-dependent relaxation timescales, indicating approximate Markovianity[51] at lag times of 20 ns or larger are shown in Extended Data Fig. 7. Reversible transition matrices were then estimated at a lag time of 20 ns. The microstates of each MSM were clustered into a set of three to four metastable states using the robust Perron cluster analysis[52]. At this resolution, the metastable states sampled by the different mutants can be clearly associated between wild-type and mutant, as shown in Fig. 3c. The Markov model was used to generate random trajectories shown in Fig. 3d as described in Ref. 23.

31. Cao, H., Garcia, F., and McNiven, M. A., Differential distribution of dynamin isoforms in mammalian cells. *Mol Biol Cell* **9**, 2595-2609 (1998).
32. Kabsch, W., XDS. *Acta Crystallogr D Biol Crystallogr* **66**, 125-132 (2010).
33. McCoy, A. J. et al., Phaser crystallographic software. *J Appl Crystallogr* **40**, 658-674 (2007).
34. Emsley, P., Lohkamp, B., Scott, W. G., and Cowtan, K., Features and development of Coot. *Acta Crystallogr D Biol Crystallogr* **66**, 486-501 (2010).
35. Adams, P. D. et al., The Phenix software for automated determination of macromolecular structures. *Methods* **55**, 94-106 (2011).
36. Chen, V. B. et al., MolProbity: all-atom structure validation for macromolecular crystallography. *Acta Crystallogr D Biol Crystallogr* **66**, 12-21 (2010).
37. The PyMOL Molecular Graphics System, Version 1.7.0.1. (Schrödinger, LLC).
38. Kabsch, W., A solution for the best rotation to relate two sets of vectors. *Acta Crystallographica Section A* **32**, 922-923 (1976).
39. Larkin, M. A. et al., Clustal W and Clustal X version 2.0. *Bioinformatics* **23**, 2947-2948 (2007).
40. Pettersen, E. F. et al., UCSF Chimera--a visualization system for exploratory research and analysis. *J Comput Chem* **25**, 1605-1612 (2004).
41. Schuck, P., Size-distribution analysis of macromolecules by sedimentation velocity ultracentrifugation and lamm equation modeling. *Biophys J* **78**, 1606-1619 (2000).
42. Laue, T. M. and Stafford, W. F., 3rd, Modern applications of analytical ultracentrifugation. *Annu Rev Biophys Biomol Struct* **28**, 75-100 (1999).
43. Laue, M. T., Shah, B. D., Rigdeway, T. M., and Pelletier , S. L., in *Analytical Ultracentrifugation in Biochemistry and Polymer Science.*, edited by S. E. H. e. al. (Royal Society of Chemistry, Cambridge, 1992), pp. 90-125.
44. Edelstein, A. et al., Computer control of microscopes using microManager. *Curr Protoc Mol Biol* Chapter: Unit14.20 (2010).
45. Humphrey, W., Dalke, A., and Schulten, K., VMD: visual molecular dynamics. *J Mol Graph* **14**, 33-38 (1996).
46. Lindahl, E., Hess, B., and van der Spoel, D., GROMACS 3.0: a package for molecular simulation and trajectory analysis. *Molecular modeling annual* **7**, 306-317 (2001).
47. MacKerell, A. D., Jr., Feig, M., and Brooks, C. L., 3rd, Extending the treatment of backbone energetics in protein force fields: limitations of gas-phase quantum mechanics in reproducing protein conformational distributions in molecular dynamics simulations. *J Comput Chem* **25**, 1400-1415 (2004).
48. Prinz, J.-H. et al., Markov models of molecular kinetics: Generation and validation. *The Journal of Chemical Physics* **134**, 174105 (2011).
49. Stanley, N., Esteban-Martin, S., and De Fabritiis, G., Kinetic modulation of a disordered protein domain by phosphorylation. *Nat Commun* **5**, 5272 (2014).
50. Senne, M. et al., EMMA: A Software Package for Markov Model Building and Analysis. *Journal of Chemical Theory and Computation* **8**, 2223-2238 (2012).
51. Swope, W. C., Pitera, J. W., and Suits, F., Describing Protein Folding Kinetics by Molecular Dynamics Simulations. 1. Theory *The Journal of Physical Chemistry B* **108**, 6571-6581 (2004).
52. Deuflhard, P. and Weber, M., Robust Perron cluster analysis in conformation dynamics. *Linear Algebra and its Applications* **398**, 161-184 (2005).
53. Chappie, J. S. and Dyda, F., Building a fission machine--structural insights into dynamin assembly and activation. *J Cell Sci* **126**, 2773-2784 (2013).

Figures

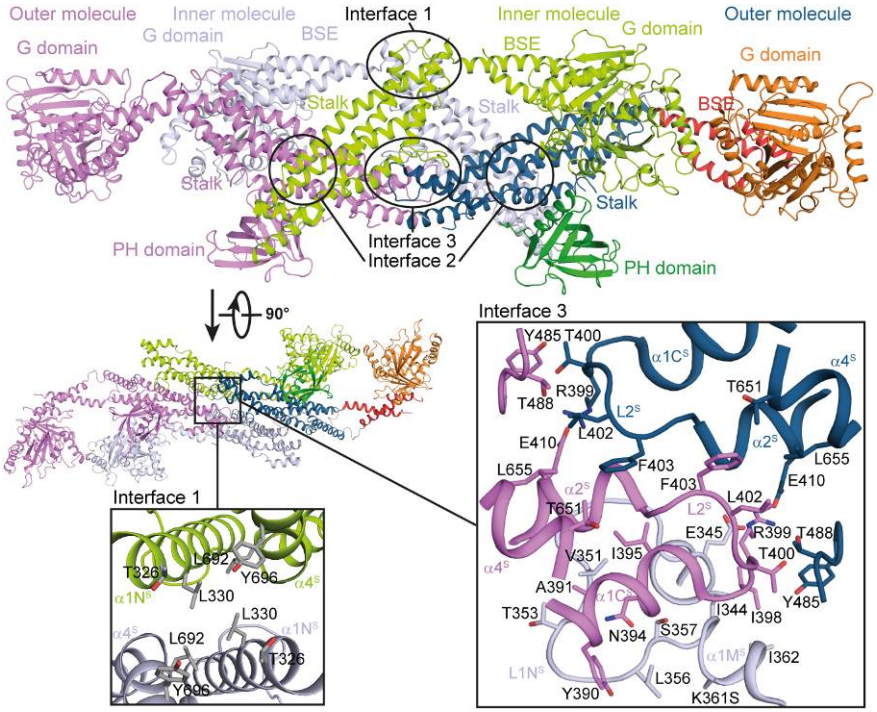

Figure 1 | Structure of the dynamin 3 tetramer.

Each molecule is separately colored, in the right molecule, individual domains are coloured. The tetramer consists of two dimers, each formed via the central interface 2. The two dimers are connected via interfaces 1 and 3 to build the tetramer. One inner molecule is omitted from the detail view for clarity.

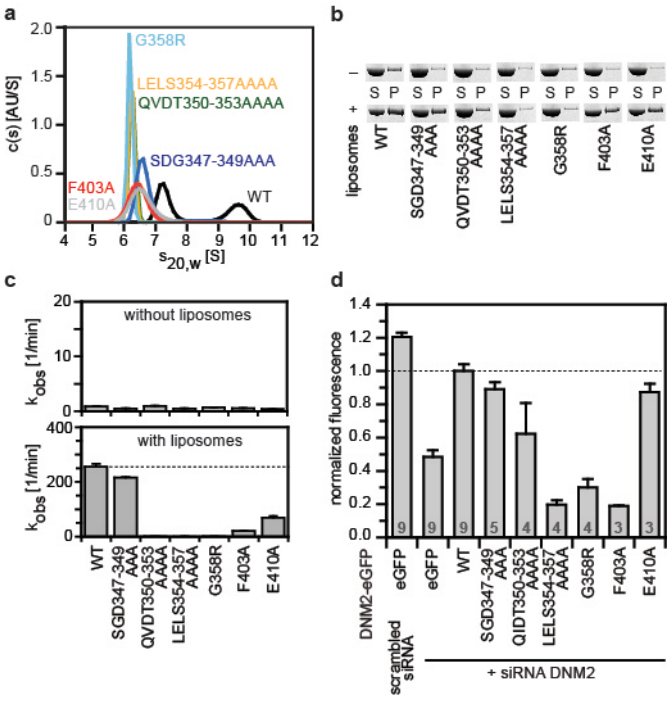

Figure 2 | Interface 3 is crucial for assembly and function of dynamin.
a, Sedimentation velocity experiments for dynamin 3 and the indicated mutants. The following molecular masses were obtained for singly sedimenting species: QVDT350-353AAAA 162 kDa; LELS354-357AAAA 164 kDa; G358R: 167 kDa. The molecular weight of the dynamin 3 construct is 86 kDa. **b**, Liposome co-sedimentation assays for dynamin 3 and the indicated mutants. S- Supernatant, P- Pellet fraction. **c**, GTPase activity for dynamin 3 and the indicated mutants in the absence and presence of liposomes. Data were measured in duplicate, error bars indicate the range of the two measurements. **d**, Capacity of dynamin 2 mutants to reconstitute defective CME in HeLa cells depleted of endogenous dynamin 2, as monitored by fluorescent transferrin uptake. Data shown represent mean±SEM, the number of independent experiments is indicated in the bar. Sequence QIDT (amino acids 350-353) in dynamin 2 corresponds to QVDT in dynamin 3.

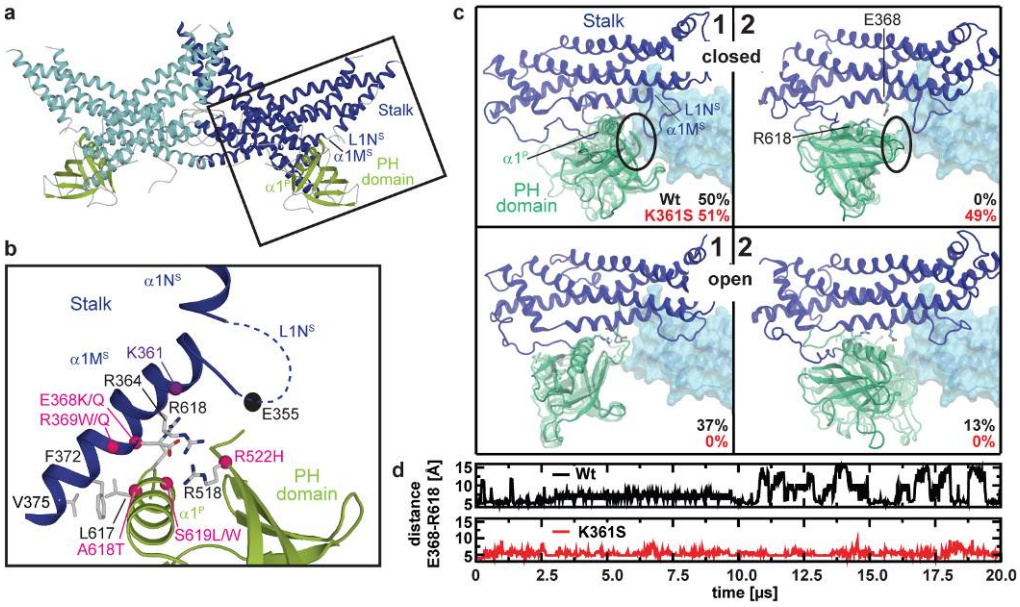

Figure 3 | Coupling of auto-inhibition and oligomerization.

a, Stalks and PH domains in the dynamin tetramer as seen in the crystal. The box defines the view displayed in **c**. **b**, Close-up view in the PH domain stalk interface from **a**. Mutations in dynamin 2 implicated in CNM are indicated as pink balls, K361 and E355 in purple and black balls, respectively. **c**, Markov state models were constructed from MD simulation data including the stalk and PH domain. For each metastable PH domain conformation, three representative structures are shown. Clashes between PH domain and assembling stalk (light blue surface) are indicated by black ovals. Percentages indicate the occurrence of each metastable state for Wt dynamin 3 (black) and the mutant K361S (red). 'Open'/'Closed': Position of the PH domain allows/inhibits oligomerization. **d**, Example trajectories. The conformational dynamics are projected onto the Glu368-Arg618 distance, which illustrates opening and closure of the PH domain at the auto-inhibited site.

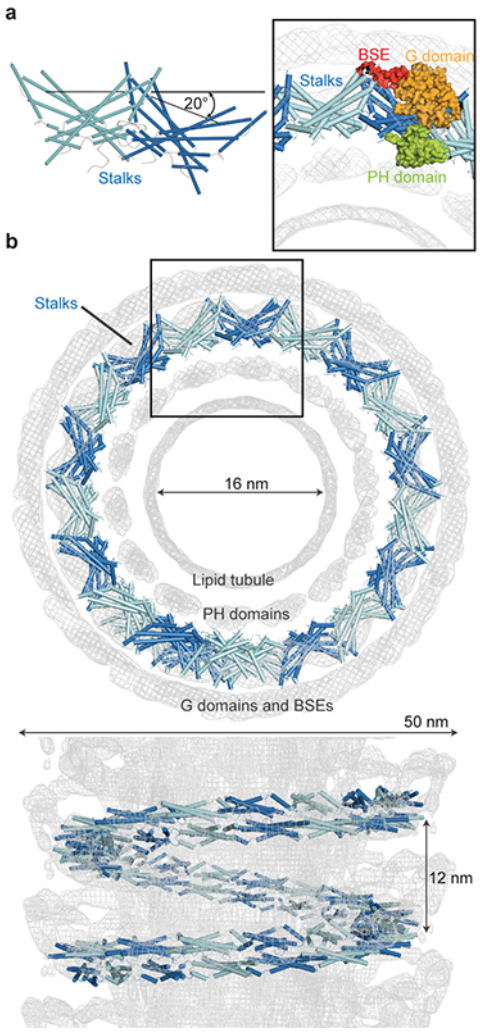

Figure 4 | Assembly of the stalks leads to a right handed dynamin helix.
a, Bent architecture of the dynamin 3 tetramer. Only the stalks helices are shown as cylinders, first dimer in light blue, second dimer in dark blue. **b**, Assembly of dynamin 3 tetramers using the geometry of interface 3 leads to a right handed helix which fits an EM map of the non-constricted dynamin 1 helix[24] (shown in mesh representation). For clarity, only the stalks are displayed. In the inset, the G domain of an inner molecule and the PH domain of the adjacent outer molecule are shown in surface representation.

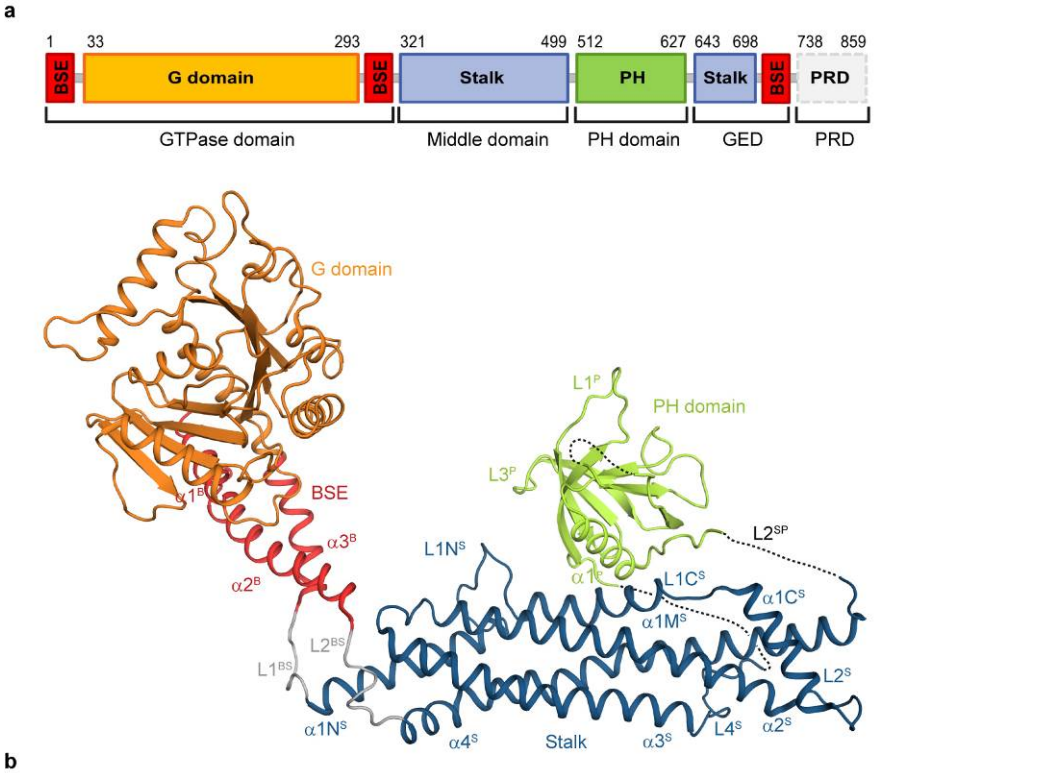
a
1
33
293
321
499
512
627
643
698
738
859
BSE
G domain
BSE
Stalk
PH
Stalk
BSE
PRD
GTPase domain
Middle domain
PH domain
GED
PRD
G domain
BSE
PH domain
L1P
L3P
L2SP
L1NS
L1CS
α1CS
α1MS
L2S
L2BS
L1BS
α1NS
α4S
Stalk
α3S
L4S
α2S

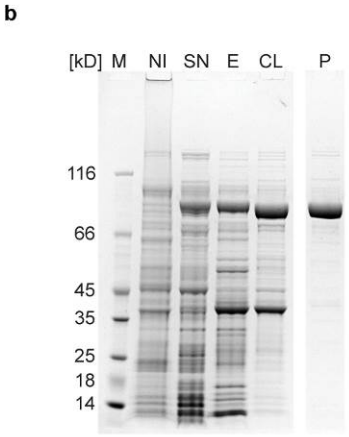
b
[kD] M
NI
SN
E
CL
P
116
66
45
35
25
18
14

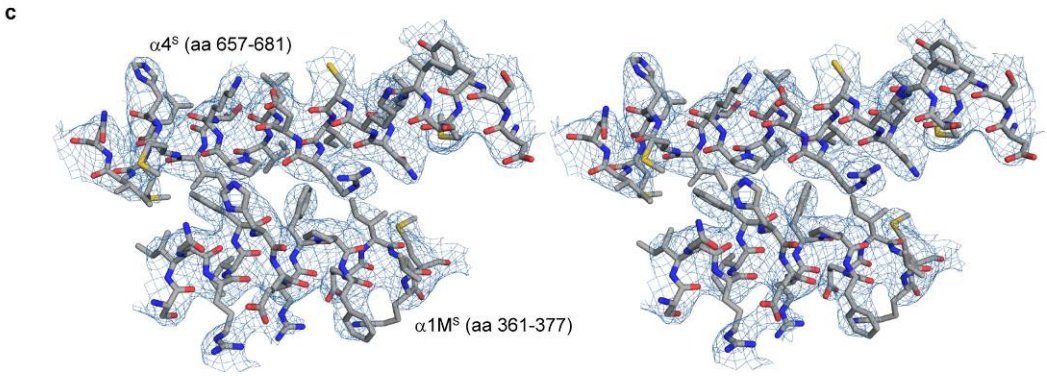
c
α4S (aa 657-681)
α1MS (aa 361-377)

Extended Data Figure 1 | Characterization of the dynamin 3 construct.

a, Top: Domain structure of dynamin 3. The previously used sequence-derived domain nomenclature is shown below. Bottom: A dynamin 3 monomer color-coded according to the domain architecture. **b**, SDS-PAGE representing a typical purification of dynamin 3: M – marker proteins, NI – whole-cell-lysate, non-induced, SN – supernatant of cleared lysate, E - elution peak of the Talon-Co^{2+} column, CL – after cleavage with TEV protease, P – pool after gelfiltration. **c**, Representative electron density map (stereo view). Shown are two stalk helices as stick model, the $2F_o$ - F_c map is contoured at 1.0 σ.

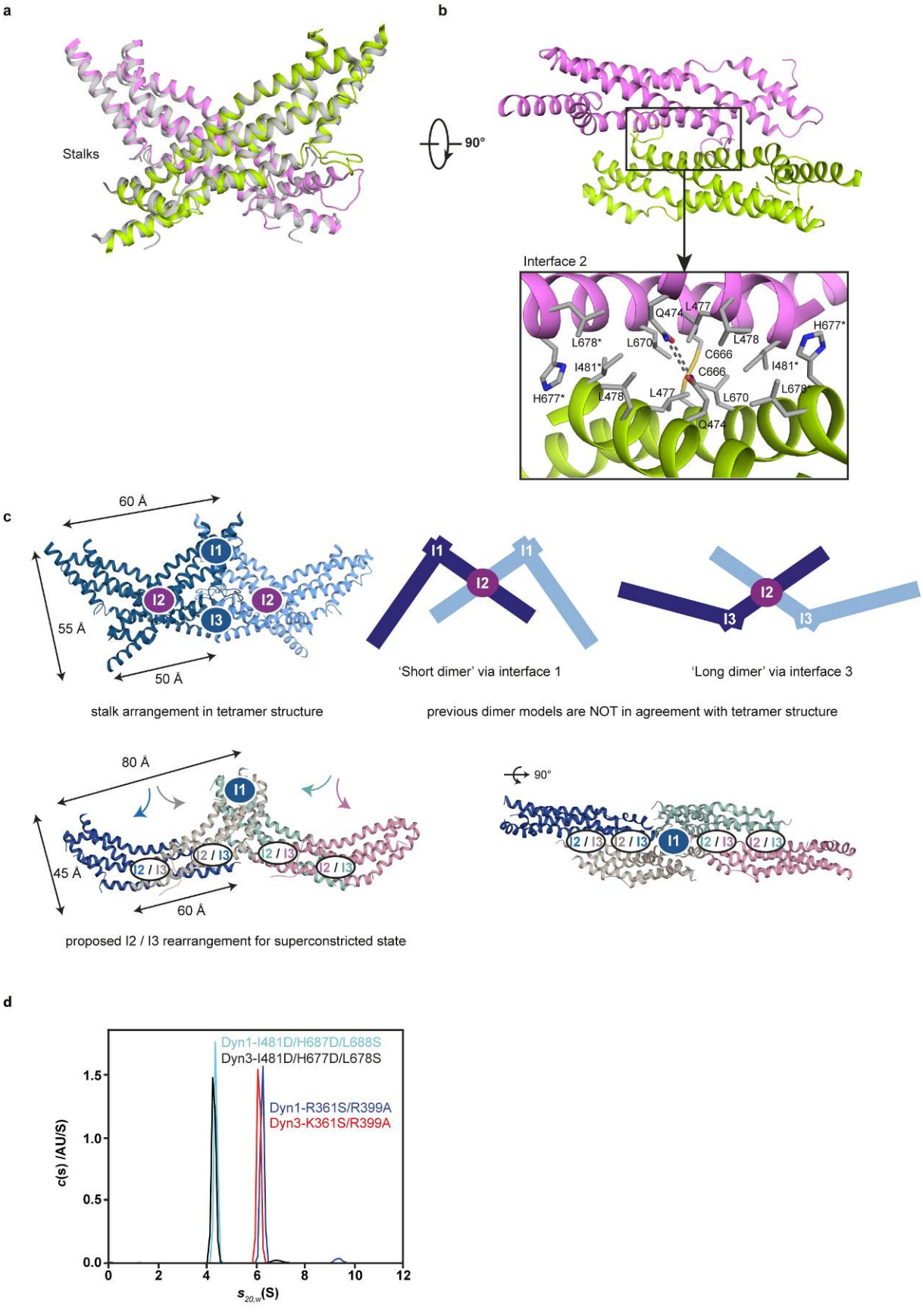
a
Stalks
b
90°
Interface 2
Q474
L477
H677*
L678*
L670
L478
C666
I481*
C666
I481*
H677*
L478
L477
L670
L678*
Q474
c
60 Å
55 Å
50 Å
I1
I2
I2
I3
stalk arrangement in tetramer structure
I1
I1
I2
'Short dimer' via interface 1
I2
I3
I3
'Long dimer' via interface 3
previous dimer models are NOT in agreement with tetramer structure
80 Å
45 Å
60 Å
I1
I2 / I3
I2 / I3
I2 / I3
I2 / I3
proposed I2 / I3 rearrangement for superconstricted state
90°
I2 / I3
I2 / I3
I1
I2 / I3
I2 / I3
d
Dyn1-I481D/H687D/L688S
Dyn3-I481D/H677D/L678S
Dyn1-R361S/R399A
Dyn3-K361S/R399A
c(s) /AU/S)
1.5
1.0
0.5
0.0
0
2
4
6
8
10
12
s20,w(S)

Extended Data Figure 2 | Dimerization of dynamin 3.

a, Superposition of dynamin 1 (grey, pdb 3SHN) and dynamin 3 (magenta and green) dimers, color code as in Fig. 1. The stalk arrangement in dynamin 3 is essentially the same as in dynamin 1. **b**, Interface 2 in dynamin 3. The view is rotated by 90° with respect to **a**. The zoom shows the side chains of residues involved in interface formation. Residues, whose mutation render dynamin 1 and dynamin 3 monomeric, are marked with an asterisk. **c**, top: Stalks of the dynamin 3 tetramer, as seen in the crystal structure (left). Dynamin dimers (dark and light blue) are formed via interface 2 (I2) and assemble into the tetramer via interfaces 1 and 3 (I1 and I3, respectively). In alternative dimerization models (middle and right)[53], dynamin monomers assemble via interface 1 (left) or interface 3 (right) to form elongated dimers of different shape. Bottom: Arrangement of stalks of a dynamin 1 as fitted into a cryo EM density map of a super-constricted dynamin 1 helix (pdb 4UUD)[26]. **d**, Oligomeric state of dimer interface mutants, as assayed by AUC at a protein concentration of 20 µM. The following molecular masses were obtained from c(s) analyses: dynamin 1-R361S/R399A (176 kDa, dimeric) in dark blue, dynamin 1-I481D/H687D/L688S (84 kDa, monomeric) in light blue, dynamin 3-K361S/R399A (165 kDa, dimeric) in red, dynamin 3- I481D/H677D/L678S (83 kDa, monomeric) in black.

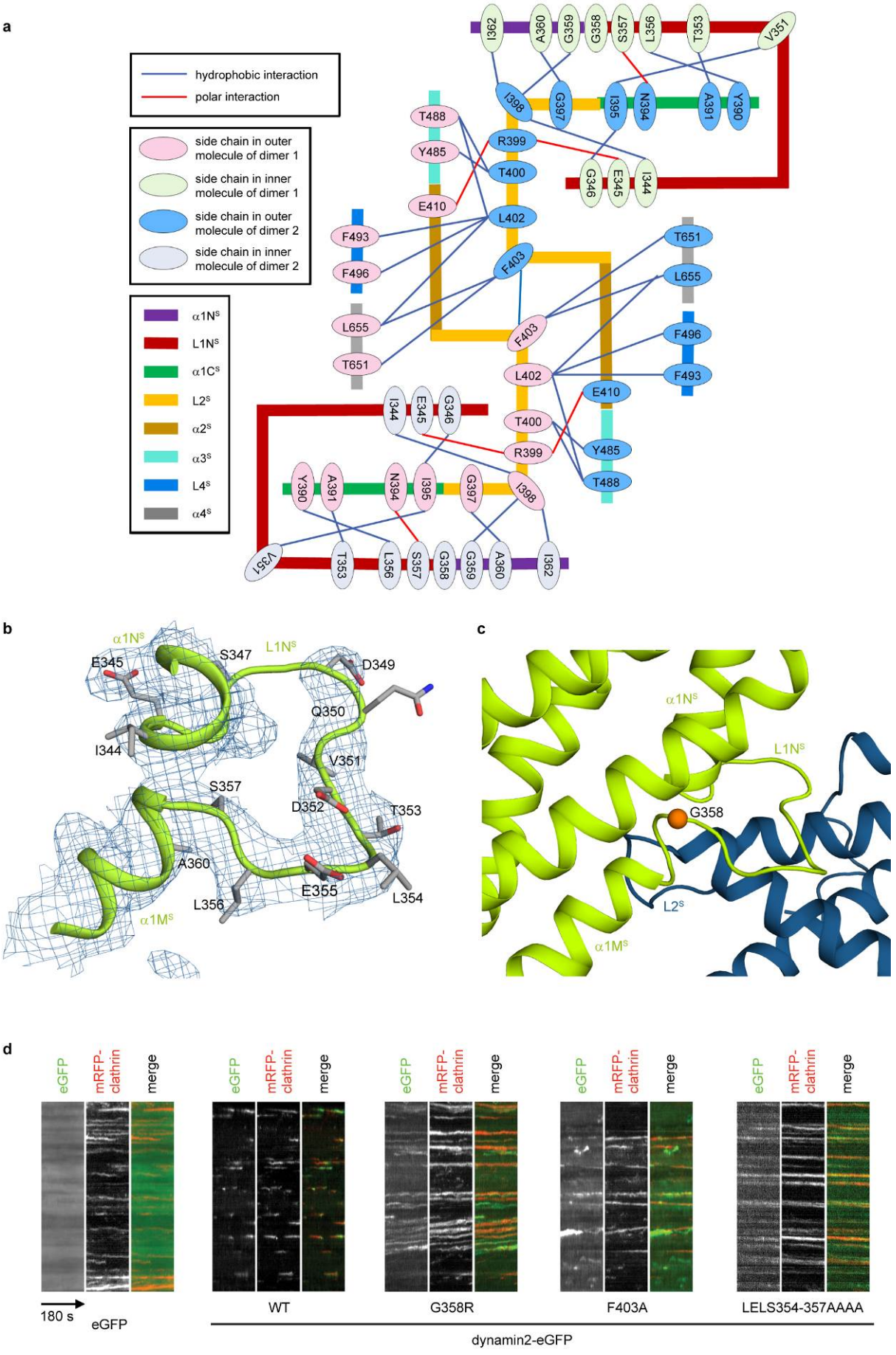
a
hydrophobic interaction
polar interaction
side chain in outer molecule of dimer 1
side chain in inner molecule of dimer 1
side chain in outer molecule of dimer 2
side chain in inner molecule of dimer 2
α1N^S
L1N^S
α1C^S
L2^S
α2^S
α3^S
L4^S
α4^S
I362 A360 G359 G358 S357 L356 T353 V351
I398 G397 I395 N394 A391 Y390
T488 Y485 R399 T400 E410 L402 F403
G346 E345 I344
F493 F496 L655 T651
T651 L655 F496 F493
F403 L402 E410 T400 R399 Y485 T488
I344 E345 G346
Y390 A391 N394 I395 G397 I398
V351 T353 L356 S357 G358 G359 A360 I362
b
α1N^S
L1N^S
E345
S347
D349
Q350
I344
V351
S357
D352
T353
A360
E355
L356
L354
α1M^S
c
α1N^S
L1N^S
G358
L2^S
α1M^S
d
eGFP
mRFP-clathrin
merge
180 s
eGFP
WT
G358R
F403A
LELS354-357AAAA
dynamin2-eGFP

Extended Data Figure 3 | Dynamin assembly via interface 3.

a, Schematic overview of the interactions in interface 3. **b**, Details of loop $L1N^S$. The $2F_o$ - F_c electron density is contoured at 1.0 σ. **c**, The CMT related mutation G358R is located at the C-terminal end of loop $L1N^S$. It likely disturbs the structural integrity of this loop and therefore might interfere with oligomerization. **d**, Clathrin-coated pit dynamics in HeLa cells expressing interface 3 mutants of dynamin 2. HeLa cells treated with dynamin2-siRNA were co-transfected with plasmids encoding eGFP / siRNA-resistant dynamin 2–eGFP and mRFP-clathrin light chain, and live cells were imaged at 37 °C by TIRF microscopy. Shown are representative time-resolved line scans (kymographs). Attenuated clathrin-coated pit dynamics upon depletion of endogenous dynamin 2 are only rescued by re-expression of Wt but not of mutant dynamin 2-eGFP. Note that the dynamin 2 mutants tested displayed a more diffuse subcellular distribution although they were still recruited to clathrin-coated pits.

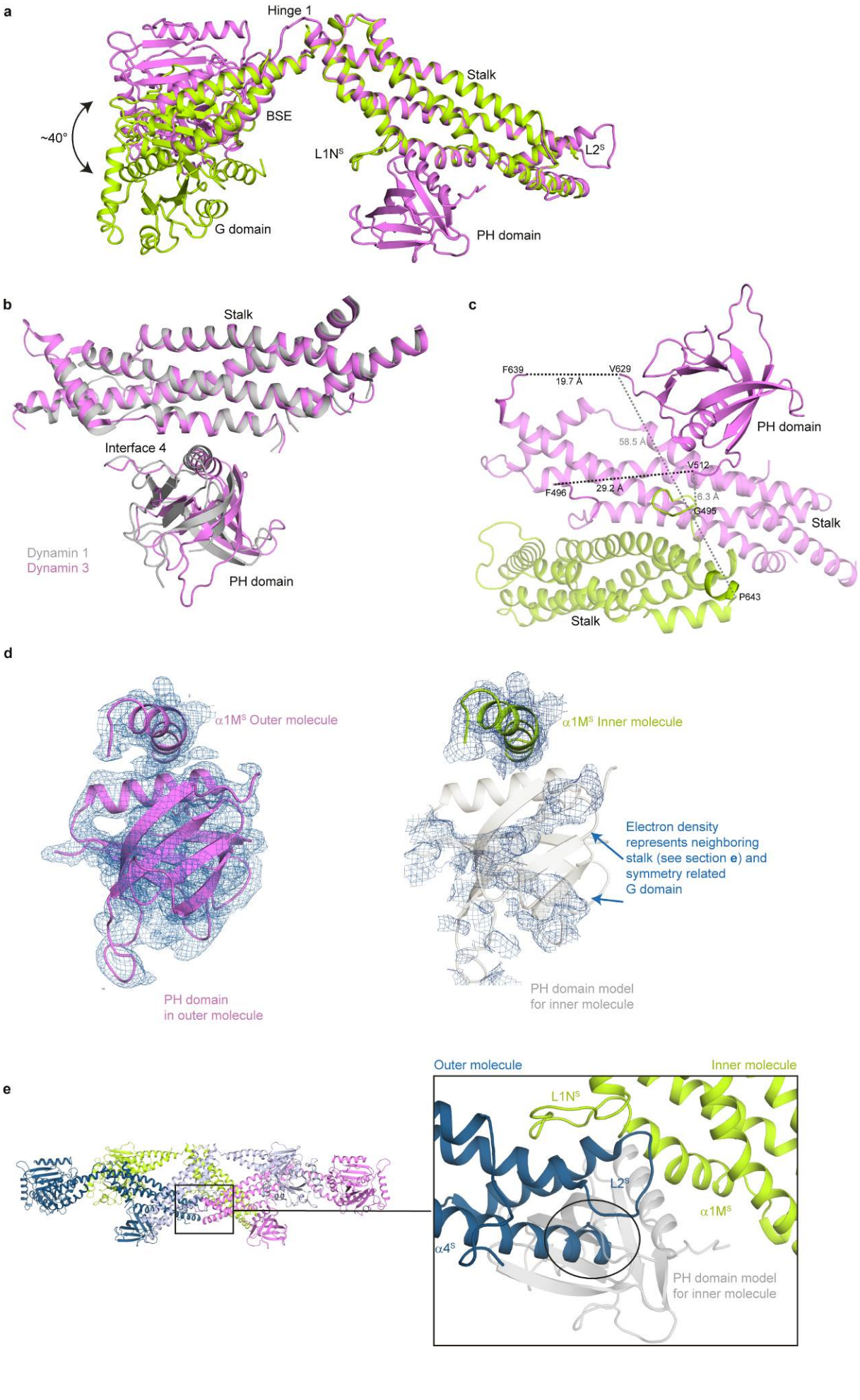
a
Hinge 1
Stalk
BSE
~40°
L1N^S
L2^S
G domain
PH domain
b
Stalk
Interface 4
Dynamin 1
Dynamin 3
PH domain
c
F639
V629
19.7 Å
PH domain
58.5 Å
V512
F496
29.2 Å
6.3 Å
G495
Stalk
P643
Stalk
d
α1M^S Outer molecule
α1M^S Inner molecule
Electron density represents neighboring stalk (see section e) and symmetry related G domain
PH domain in outer molecule
PH domain model for inner molecule
e
Outer molecule
Inner molecule
L1N^S
L2^S
α1M^S
α4^S
PH domain model for inner molecule

Extended Data Figure 4 | Localization of the PH domain in the tetramer.

a, Superposition of an outer dynamin molecule (magenta) and an inner molecule (green) of the dynamin 3 tetramer. The comparison reveals a ~40° rotation of the G domains and BSEs. Furthermore, the PH domain is visible only in the outer molecule. **b**, Superposition of stalk and PH domain in dynamin 1 (grey) and dynamin 3 (magenta). **c**, Connectivity of PH domain and stalk in the outer molecule. Shown are stalk and PH domain of an outer molecule (magenta) and the stalk of the corresponding inner molecule (green) from a dimer. Since the gap of ~58 Å between V629 of the PH domain and P643 of the inner stalk is too large to be spanned by the missing 13 residues (grey dashed line), we can unambiguously assign the PH domains in dynamin 3 to the outer stalks (black dashed lines). All other potential connections including molecules from the second dimer or symmetry-related tetramers span even larger distances (not shown). In the crystal structures of dynamin 1, an unequivocal assignment of the PH domain to a specific stalk was not possible, due to the long unresolved linker regions between the stalk and the PH domains. Concomitantly, the impact of the interface between stalk and PH domain has not been generally recognized[53]. **d**, The outer PH domains are clearly defined in the electron density (left panel), whereas no density for a PH domain is observed in the equivalent position at the inner stalks (right panel). The density visible in the right panel corresponds mainly to a G domain from a symmetry-related molecule. The $2F_o$ - F_c electron density is contoured at 1.0 σ. **e**, Modelling of a PH domain (grey) relative to an inner stalk (green) in the same geometry as seen in the outer molecules leads to steric clashes (black oval) with an adjacent stalk (blue).

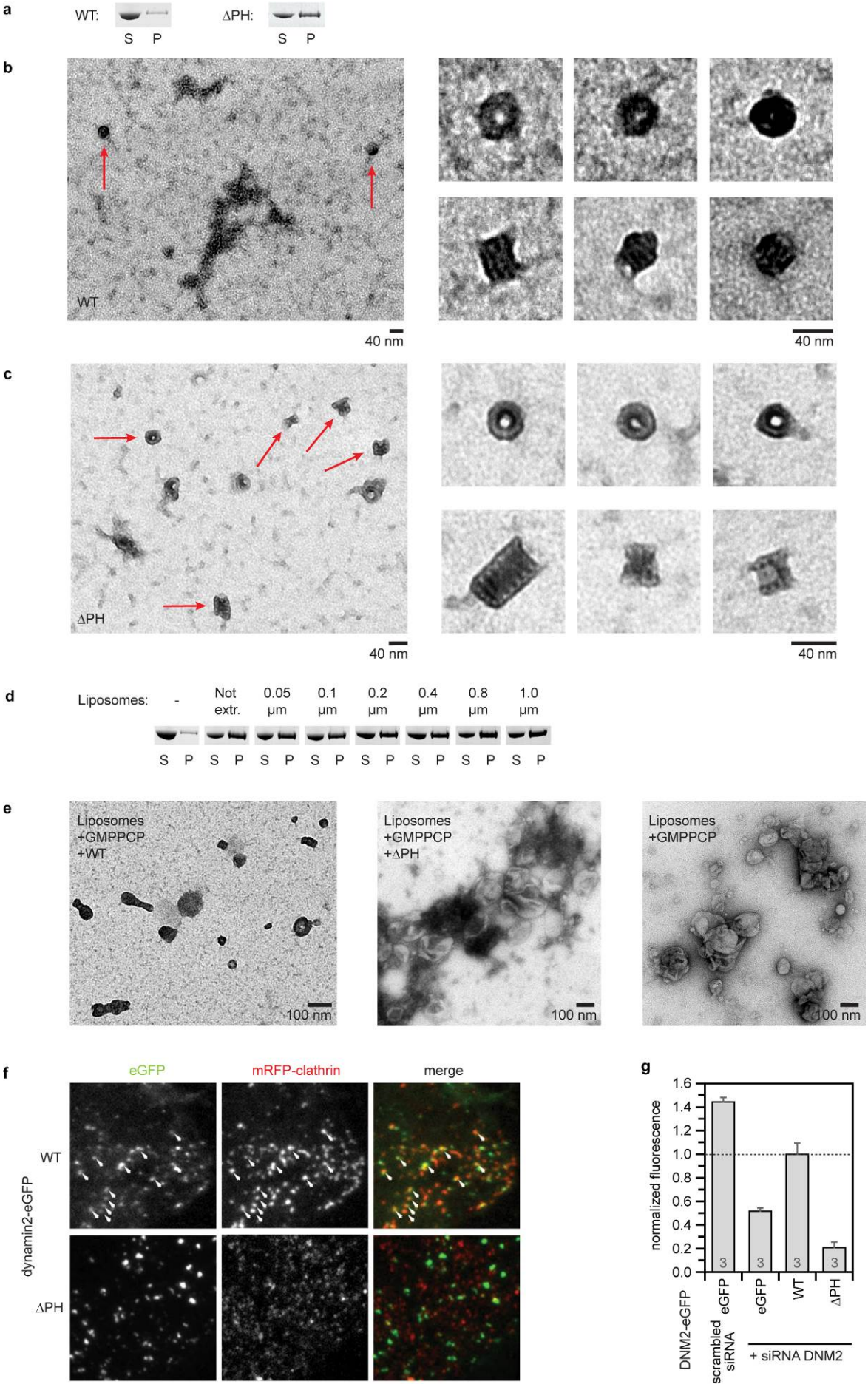
a
WT:
S P
ΔPH:
S P
b
WT
40 nm
40 nm
c
ΔPH
40 nm
40 nm
d
Liposomes:
-
Not extr.
0.05 μm
0.1 μm
0.2 μm
0.4 μm
0.8 μm
1.0 μm
S P S P S P S P S P S P S P S P
e
Liposomes +GMPPCP +WT
100 nm
Liposomes +GMPPCP +ΔPH
100 nm
Liposomes +GMPPCP
100 nm
f
eGFP
mRFP-clathrin
merge
dynamin2-eGFP
WT
ΔPH
g
normalized fluorescence
1.6
1.4
1.2
1.0
0.8
0.6
0.4
0.2
0.0
3
3
3
3
DNM2-eGFP
scrambled siRNA
eGFP
eGFP
WT
ΔPH
+ siRNA DNM2

Extended Data Figure 5 | The PH domains regulate oligomerization of dynamin.

a, A dynamin 3 variant lacking the PH domain (ΔPH) was sedimented more efficiently than Wt dynamin 3 (WT). ΔPH and WT lacked the PRD. The proteins were sedimented by ultracentrifugation after 20 h of incubation at low salt (60 mM NaCl) in the presence of the non-hydrolysable GTP analogue GMPPCP. **b, c**, Representative negative-stain electron micrographs of WT (**b**) and ΔPH (**c**) under the same conditions as in (**a**). Both constructs showed oligomeric ring structures, similar to structures seen for full-length dynamin[7]. Our data indicate that oligomerization of dynamin does not require membrane binding, but membrane binding requires oligomerization (Fig. 2). **d**, In liposome co-sedimentation assays dynamin 3 bound to Folch liposomes independently of their size. **e**, At physiological salt concentrations (150 mM NaCl), dynamin 3 efficiently tubulated unfiltered Folch liposomes. In contrast, ΔPH did not decorate the liposome surface and did not induce liposome tubulation. **f**, When expressed in HeLa cells, dynamin 2(ΔPH) formed large cytosolic aggregates that did not co-localize with mRFP-clathrin. **g**, Dynamin 2(ΔPH) was dominant-negative in transferrin uptake assays.

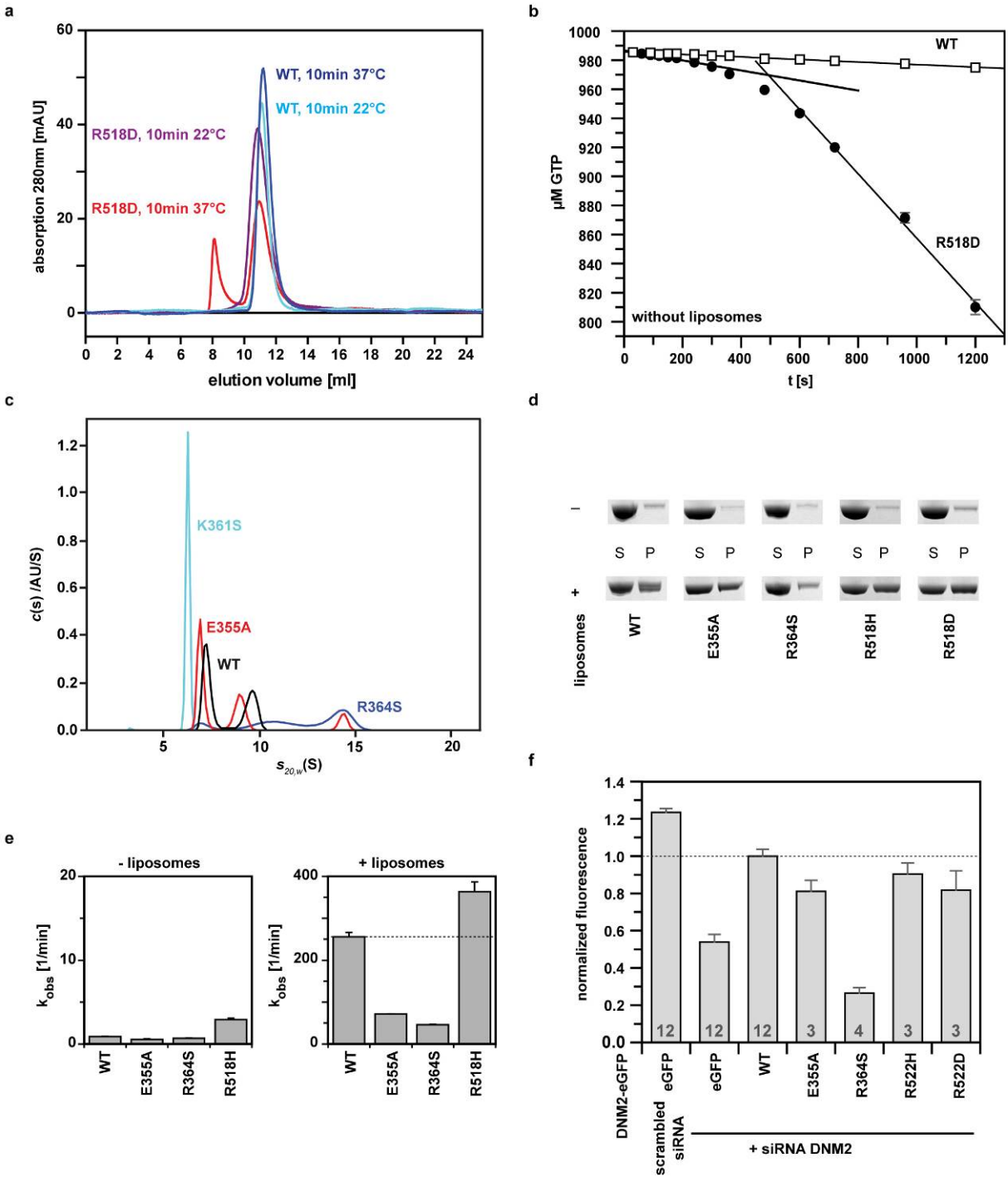

Extended Data Figure 6 | Mutational analysis of the interface between PH domain and stalk.

a, Analytical gelfiltration analysis for Wt dynamin 3 and the mutant R518D. The proteins were pre-incubated for 10 min at 22 °C or at 37 °C. When pre-incubated at 37 °C, only R518D showed a higher molecular weight species. **b**, Intrinsic GTPase activity of Wt dynamin 3 and the mutant R518D at 37 °C in the absence of liposomes. The lines represent

linear fits of GTP hydrolysis versus time. For R518D, a biphasic behaviour of the GTPase activity was apparent (for Wt: k_{obs}= 0.5 min^{-1}; for R518D: k_{obs1}= 2.2 min^{-1} and k_{obs2}= 13.3 min^{-1}). This biochemical behaviour is reminiscent to dynamin 1 mutants in the PH domain-stalk interface that show increased oligomerization and GTPase rates when incubated at 37 °C[20]. Perturbations in this interface appear to promote oligomerization of dynamin pointing to an auto-inhibitory function of this interface for oligomerization. **c**, Analytical ultracentrifugation experiments for the indicated dynamin 3 variants, as in Fig. 2a. For the mutant K361S that sediments as a single species, a molecular mass of 164 kDa could be obtained from c(s) analysis, indicating that this mutant forms dimers in solution. **d**, Liposome co-sedimentation analysis for the indicated mutants. S- Supernatant, P- Pellet fraction. **e**, GTPase activity of the indicated mutants in the absence and presence of liposomes. **f**, Ability of dynamin 2 mutants to rescue defective CME of transferrin in absence of endogenous dynamin 2. The assay was performed as described in Fig. 2d. R518 in dynamin 3 corresponds to R522 in dynamin 2 and the R522H mutation in dynamin 2 is implicated in CNM. Note: We generally observed that the GTPase experiments were the most sensitive indicators of structural perturbations induced by mutations. Compared to membrane binding assays, GTPase assays appear to be more sensitive to the actual architecture of the dynamin oligomer and alterations induced by point mutations. Transferrin uptake assays could be influenced by cellular factors, such as BAR-domain protein that may stabilize mutant dynamin forms with deficits in oligomerization.

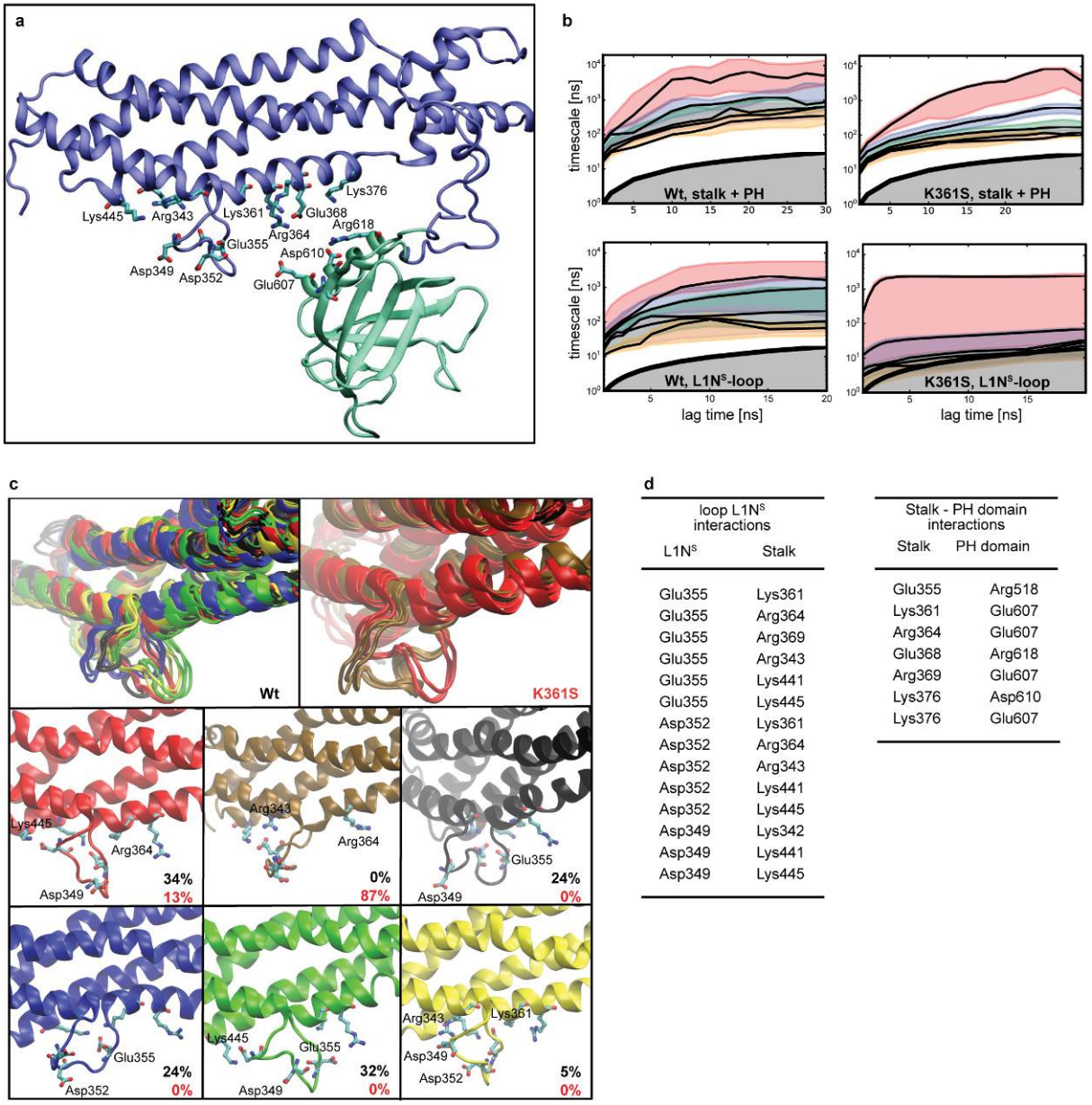

d

loop L1N^S interactions

L1N^S	Stalk
Glu355	Lys361
Glu355	Arg364
Glu355	Arg369
Glu355	Arg343
Glu355	Lys441
Glu355	Lys445
Asp352	Lys361
Asp352	Arg364
Asp352	Arg343
Asp352	Lys441
Asp352	Lys445
Asp349	Lys342
Asp349	Lys441
Asp349	Lys445

Stalk - PH domain interactions

Stalk	PH domain
Glu355	Arg518
Lys361	Glu607
Arg364	Glu607
Glu368	Arg618
Arg369	Glu607
Lys376	Asp610
Lys376	Glu607

Extended Data Figure 7 | Molecular dynamics simulations and Markov models.

a, The PH domain stalk interaction is characterized by a number of mainly polar interactions. The represented conformation is one of the starting structures (setup 2) for the MD simulations and quickly converts into one of the metastable conformations shown in Figure 3. **b**, Relaxation timescales of different constructs as a function of lag time computed from Markov models. The timescales of all models (black) have converged at a lag time of about 20 ns within statistical uncertainty (color-shaded regions), indicating approximate Markovianity. The grey area indicates the region with lag times larger than relaxation timescales. **c**, Top: intrinsic conformation dynamics of the L1N^S loop shown for the wild-type (black) and the mutant K361S (red). Bottom: Six metastable conformations and their equilibrium probabilities of the L1N^S loop (setup 3) for the wild-type (black) and mutant

K361S (red) computed from the Markov model. **d**, Residue pairs used to characterize the $L1N^S$ loop and stalk-PH domain interactions.

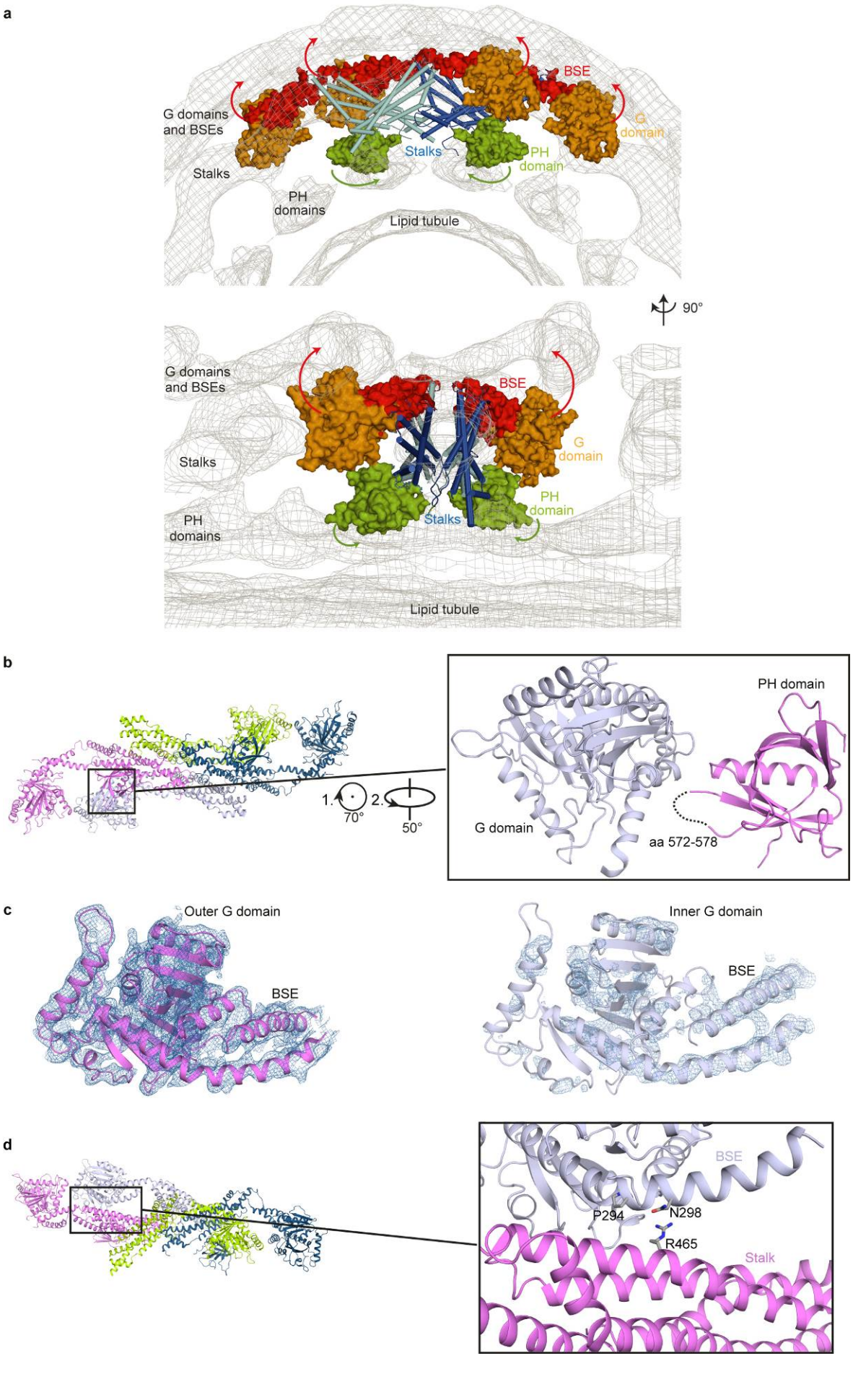
a
G domains
and BSEs
Stalks
PH
domains
BSE
G
domain
Stalks
PH
domain
Lipid tubule
90°
G domains
and BSEs
Stalks
PH
domains
BSE
G
domain
PH
domain
Stalks
Lipid tubule
b
1.
70°
2.
50°
PH domain
G domain
aa 572-578
c
Outer G domain
BSE
Inner G domain
BSE
d
BSE
P294
N298
R465
Stalk

Extended Data Figure 8 | Interactions of the G domain, stalk and BSE in the tetramer.

a, Two views on a fitting of the dynamin 3 tetramer crystal structure into the EM density of non-constricted oligomerized dynamin 1[24]. Note: The positions of the inner G domains are shown in all four molecules since the outer G domains in our crystals are stabilized by crystal contacts. Apparently, membrane binding and oligomerization is associated with major movements of the G domain, BSE and the PH domain (indicated by arrows). **b**, A loop of the outer PH domain and an inner G domain are in close proximity. **c**, The outer G domains (left), but not the inner G domains (right) are well defined in the electron density. The $2F_o$ - F_c electron density is contoured at 1.0 σ. The weak electron density for the inner G domains and the resulting uncertainty in determining the contact sites prevented us from analyzing this interaction in more detail. **d**, The BSE of an inner monomer (grey) interacts with the stalk of an outer monomer (magenta). This contact involves R465 which is mutated to tryptophan in some CNM patients. The R465W mutation leads to hyperactive dynamin[4] that fragments the T tubule network in mouse-myoblast derived myotubes and *Drosophila* body wall muscle (Ya-Wen Liu, personal communication).

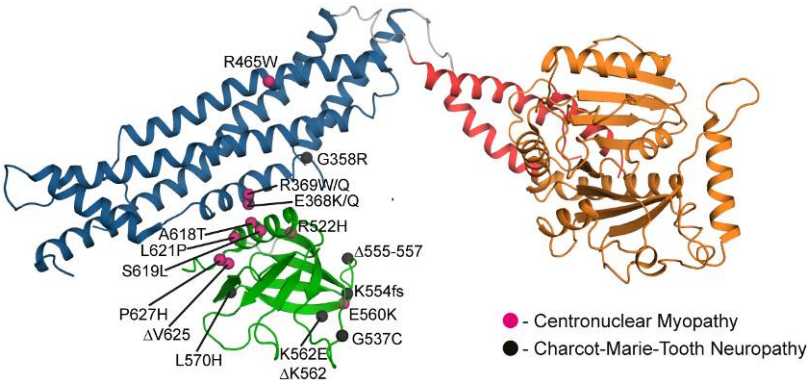

Extended Data Figure 9 | Disease-relevant mutations in dynamin.

Localizations of mutations leading to CMT disease (black balls) and CNM (pink balls) are plotted onto a dynamin 3 monomer.

Data collection	
Space group	$P2_12_12_1$, 1 tetramer / ASU
Cell dimensions	
a, *b*, *c* (Å)	97.70, 98.00, 401.52
Resolution (Å)*	3.70 (3.70-3.80)
R_{sym} (%)*	7.0 (130)
$<I/\sigma(I)>$ *	16.6 (1.8)
Completeness (%)*	99.6 (99.3)
Redundancy	7.3
Refinement	
Resolution (Å)	49.47 – 3.7
No. reflections	42,058
R_{work} / R_{free} (%)	23.2 / 27.8
No. of protein atoms	18,654
averaged B-factor protein ($Å^2$)	212
R.m.s deviations	
bond lengths (Å)	0.004
bond angles (°)	0.889

* Data in highest resolution shell are indicated in parenthesis.

Extended Data Table 1 | Data collection and refinement statistics